



Facile synthesis of hierarchically meso/nanoporous s- and c-codoped TiO₂ and its high photocatalytic efficiency in H₂ generation

Hongwei Bai, Keith Shan Yao Kwan, Zhaoyang Liu^{*}, Xiaoxiao Song, Siew Siang Lee, Darren Delai Sun^{*}

School of Civil & Environmental Engineering, Nanyang Technology University, Singapore 639798, Singapore

ARTICLE INFO

Article history:

Received 7 July 2012

Received in revised form 6 September 2012

Accepted 19 September 2012

Available online 29 September 2012

Keywords:

Hierarchically meso/nanoporous structure

H₂ generation

Photocatalysis

S- and C-codoped TiO₂

ABSTRACT

Here, hierarchically meso/nanoporous TiO₂ was successfully fabricated by a facile and efficient hydrolysis and calcination method using Ti(OC₄H₉)₄ and K₂S₂O₈ as precursors. The hydrosol was firstly prepared by drop-wise adding ethanol dissolved Ti(OC₄H₉)₄ solution into acetone dissolved K₂S₂O₈ solution under a vigorous stirring and heating condition. After being sufficiently hydrolyzed, the hydrosol was calcined to promote the crystallization of TiO₂ and successfully dope S and C on TiO₂. The calcination temperature significantly affects the doping of S and C on TiO₂, crystallization of TiO₂, formation of hierarchically meso/nanoporous structure of TiO₂ and its light absorption capability. The S- and C-codoped TiO₂ exhibits high photocatalytic H₂ generation efficiency in a water/methanol sacrificial reagent system under the irradiation of UV light. The high photocatalytic efficiency is dependent on the comprehensively competing effects of the codoping of S and C, crystallization, specific surface area and light absorption capability. The S- and C-codoped TiO₂ calcined at 600 °C demonstrates the highest photocatalytic H₂ generation efficiency, which is ascribed to the balanced synergy of the abovementioned factors.

© 2012 Elsevier B.V. All rights reserved.

1. Introduction

The well-known issues related to environmental pollution and global warming concerns have motivated numerous efforts concentrating on photocatalytic H₂ generation to utilize abundant clean energy [1,2]. H₂ energy is an ideal candidate to alleviate the overdependence on fossil fuels in future because of its high energy intensity, environmental friendliness, and recycling possibility [2–4]. Since the benchmark paper published on Nature in 1972 reporting the photocatalytic water splitting on titania electrodes under UV light irradiation [5], it becomes a promising and sustainable approach to use TiO₂ photocatalytic water splitting to generate H₂. Owing to its unique properties including suitable band position, non-toxicity, biological and chemical stability in solution, and high photocatalytic efficiency [6,7], TiO₂ has essentially demonstrated to be one of the most efficient and viable photocatalyst [7–11]. In the past decades, huge research efforts were undertaken to fundamental research and practical applications of TiO₂ for clean energy generation and environmental purifications, etc [12–17].

However, the large band gap of 3.2 eV (anatase) restricts that TiO₂ can only absorb the UV fraction of solar light (about 2–3% of the total solar energy) to generate electron–hole pairs, which

will migrate from the conduction and valence bands to the surface of TiO₂ to respectively initiate reductive and oxidative reactions [6,8,18]. The poor light absorption capability to generate electrons and holes as well as their fast recombination result in comparatively-low photocatalytic activity of TiO₂ [19,20]. Therefore, it is still challengeable to widely apply TiO₂ for large-scale clean energy generation and practical environmental purification in a cost-effective and efficient way [19,20]. Photosensitized TiO₂ by doping inorganic element such as hydrogen [20], carbon [21–24], sulfur [25], and nitrogen [1,11,18,26–28] proved to be an effective approach to tackle this challenge, as these doped elements act as electron donor or acceptor in the forbidden band of TiO₂ thus inducing absorption in the visible region [18]. A merit for carbon doping is that it can significantly stabilize the photoactive anatase TiO₂, inhibit the sintering of nanocrystals and expedite the adsorption of organic pollutant molecules by catalysts [6,24,29]. At the same time, the good conductivity of carbon also makes it possible that the carbon doped TiO₂ would accelerate the charge transfer from bulk of TiO₂ to the desired location where oxidation reactions take place [6,30]. Similar to the merits of inorganic element doping, the Pt deposition on the surface of TiO₂ would enhance the separation of photogenerated electrons and holes to prolong their lifespan, and suppress the reverse reaction between H₂ and O₂ so as to lead to improve the photocatalytic activity of TiO₂ [31].

Besides, considering the significance of the microstructure on the performance of photocatalyst, it is very interesting to search for new photocatalyst with an appropriate crystal structure and

^{*} Corresponding author. Tel.: +65 6790 6273; fax: +65 6791 0676.

E-mail addresses: zyliu@ntu.edu.sg (Z. Liu), ddsun@ntu.edu.sg (D.D. Sun).

high specific surface area to improve the photocatalytic activity [14,32–36]. Porous TiO_2 with large specific surface area would ease the adsorption and encourage the accessibility of reactants to the catalysts via providing enough active sites [8,37,38]. Furthermore, the porous nanosized TiO_2 photocatalyst also allows multiple scattering and reflection of light so as to urge its light absorption capability [39,40].

In this study, a facile hydrosol and calcination method is developed to fabricate hierarchically meso/nanoporous S- and C-codoped TiO_2 to integrate the above mentioned virtues to synergistically improve the photocatalytic activity, which was witnessed by its photocatalytic H_2 generation activity in a water/methanol sacrificial reagent system under the irradiation of UV light. Furthermore, the effect of Pt loading on photocatalytic H_2 generation activity of the hierarchically meso/nanoporous S- and C-codoped TiO_2 will also be investigated.

2. Experimental

2.1. Materials synthesis

Except stated elsewhere, all chemicals were from Sigma–Aldrich with reagent grade and used directly without further purification. Deionized (DI) water (Millipore, USA) with a conductivity reaching $18 \Omega \text{m/cm}$, acetone and ethanol were used as solvents for the materials synthesis. In brief, a typical procedure for the fabrication of S- and C-codoped TiO_2 was described. Firstly, $0.5 \text{ g K}_2\text{S}_2\text{O}_8$ (the S source) was added into 20 mL of absolute acetone and stirred for 5 min . Then the suspension was added drop-wisely into 100 mL DI water (60°C) under vigorous stirring. The mixed solution was continuously stirred for 30 min before cooling down to room temperature (solution A) [6]. Secondly, $10 \text{ mL Ti}(\text{OC}_4\text{H}_9)_4$ (Merck, Germany) was added into 20 mL of absolute ethanol and stirred for 5 min to ensure the formation of clear and homogeneous solution (solution B). This solution B was added drop-wisely into 40 mL of above prepared solution A under vigorous stirring. The subsequently formed white suspension was continuously stirred for 120 min to allow sufficient hydrolysis and reaction. The suspension was withdrawn and centrifuged at 6000 rpm for 5 min to discard the supernatant. The precipitates were thoroughly washed with DI water before calcination at different temperatures from 200°C to 800°C in air for 180 min . The S- and C-codoped TiO_2 calcined at different temperatures was designated as TSC-T, where -T indicates the calcination temperatures ($^\circ\text{C}$), for example TSC-200, TSC-400, TSC-500, TSC-600 and TSC-800 indicate the S- and C-codoped TiO_2 calcined at 200°C , 400°C , 500°C , 600°C and 800°C , respectively. Particularly, the uncalcined S- and C-codoped TiO_2 was designated as TSC-0.

As Pt loading on the surface of TiO_2 is widely reported to be a useful technique to enhance the photocatalytic activity of pure TiO_2 , therefore we also prepared $0.5\% \text{ Pt/TiO}_2$ catalyst via loading Pt on the surface of previously synthesized hierarchically meso/nanoporous TSC-600 by using a photodeposition method [31,41]. In brief, a mixed solution of H_2PtCl_6 and TSC-600 was prepared under sonication. Afterwards, the suspension was illuminated under UV light (UVP Lamp, UK) overnight at room temperature [37]. Finally, the precipitate was filtrated, washed by DI water and dried at 120°C for 8 h in an electronic oven. The light gray color of the prepared $0.5\% \text{ Pt/TiO}_2$ catalyst indicates that the Pt was successfully deposited on the surface of TiO_2 [31].

2.2. Characterization

The morphology of the prepared samples was observed by field emission scanning electron microscopy (FESEM) (Jeol, JSM

Table 1

Binding energy (eV), fwhm of the TSC-600.

Position (fwhm)			Position (fwhm)		Position (fwhm)		Position (fwhm)	
C 1s			O 1s		S 2p		Ti 2p3/2	Ti 2p1/2
284.6	286.06	288.49	528.95	531.74	168.91	457.84	463.52	
(1.31)	(1.03)	(0.84)	(1.14)	(2.98)	(3.86)	(1.06)	(1.72)	

7600F) and transmission electron microscope (TEM) (Jeol, JEM-2010) with an accelerating voltage of 200 kV . An energy dispersive X-ray spectrometer (EDS) detector (Oxford, 80 mm^2) attached to the FESEM was used to measure the element composition and distribution of the prepared samples. The chemical composition and electron structure of the prepared samples were measured by a Kratos axis ultra X-ray photoelectron spectrometer (XPS) with a monochromatic Al $\text{K}\alpha$ source at 1486.7 eV , at a voltage of 15 kV and an emission current of 10 mA . The carbonaceous C 1s line of 284.6 eV was applied as the reference to calibrate the binding energies (eV). The structure and crystal phase of the prepared samples were analyzed by powder X-ray diffractometer (XRD, Bruker AXS D8 advance) with monochromated high-intensity Cu $\text{K}\alpha$ radiation ($\lambda = 1.5418 \text{ \AA}$) operated at 40 kV and 30 mA . Ultraviolet–visible (UV–vis) diffuse reflection spectra of the prepared samples were recorded by a Thermo Scientific Evolution 300 UV–vis spectrometer (Thermo Fisher Scientific, Massachusetts, USA) equipped with an integrating sphere assembly and a Xenon lamp source. The porous structures of the prepared samples were characterized by N_2 adsorption/desorption isotherms using a Micromeritics ASAP 2040 system at liquid nitrogen temperature (77 K). Before the measurement, 0.1 g sample was out-gassed under vacuum for 6 h at 250°C . Pore volume and diameter distributions were derived from the desorption branches of the isotherms by the Barrett–Joyner–Halenda (BJH) model, and the Brunauer–Emmett–Teller (BET) specific surface areas were calculated from the linear parts of the BET plots.

2.3. Evaluation of photocatalytic H_2 generation activity

The photocatalytic H_2 generation test of the prepared samples was carried out in an inner irradiation type Pyrex reactor with a volume of 270 mL with a 400 W high pressure Hg lamp (Riko, UVL-400HA) as the light source. The reactor was wrapped by a cooling water jacket with re-circulating tap water to maintain a constant reactor temperature of 298 K . The prepared sample at a dosage of 0.5 g/L was suspended into the mixed methanol/water solution on a magnetic stirrer to form homogeneous reaction solution. Prior to irradiation, the reactor was purged thoroughly with nitrogen gas for 30 min to de-aerate the reactor. The H_2 gas generated from the photocatalytic reaction was collected by a water replacement trap and was analyzed using a TCD-type gas chromatography (Agilent 7890A, HP-PLOT MoleSieve/5A) [42,43]. The photocatalytic H_2 generation activity of the well prepared $0.5\% \text{ Pt/TSC-600}$ was also evaluated using the same method as above.

3. Results and discussion

The chemical composition, electronic structure and the presence of elements in the prepared TSC-T was measured by XPS. Here, the TSC-600 was taken as a typical example to do the detailed analysis about its XPS survey spectra (Fig. 1a) and high resolution spectrum of Ti 2p (Fig. 1b), S 2p (Fig. 1c), C 1s (Fig. 1d) and O 1s (Fig. 1e). The detailed binding energies and full width at half maximum (fwhm) of those elements were listed in Table 1. The XPS survey spectra in Fig. 1a reveal that the TSC-600 contains Ti, O, S and C. The high resolution Ti 2p spectra (Fig. 1b) exhibits two typical

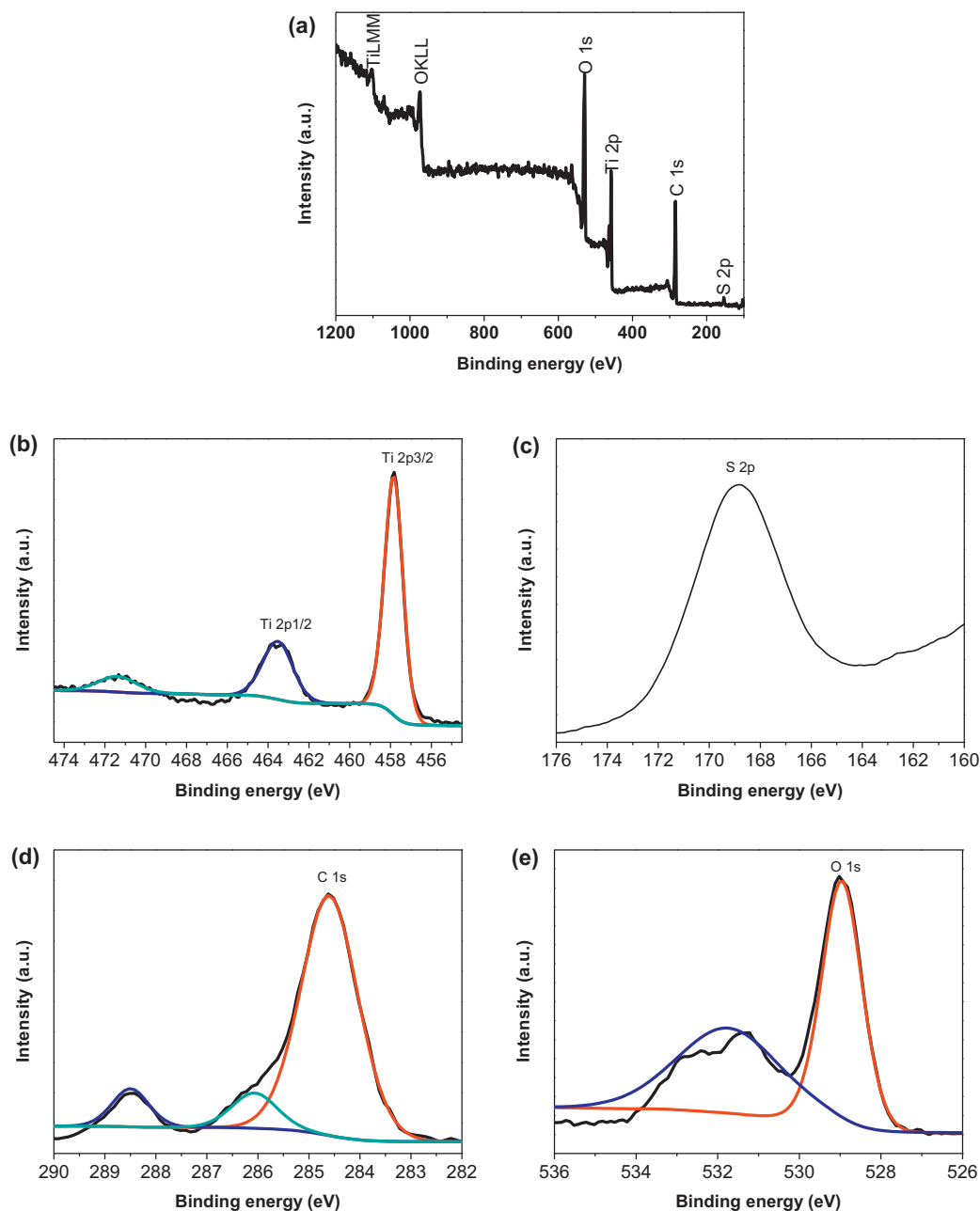


Fig. 1. (a) XPS survey spectra, and high resolution XPS spectrum, (b) Ti 2p, (c) S 2p, (d) C 1s and (e) O 1s of the TSC-600.

peaks corresponding to binding energies of 457.84 eV (Ti 2p_{3/2}) and of 463.52 eV (Ti 2p_{1/2}). The slight shift of Ti 2p_{3/2} peak with respect to that of Ti⁴⁺ in pure anatase TiO₂ (458.5–459.7 eV) indicates the presence of Ti³⁺ [6]. The high resolution spectra of S 2p in Fig. 1c further confirms the presence of S, and only one peak appeared at 168.91 eV [25]. The peak at 168.91 eV can be ascribed to the sulfur substituting titanium atoms in the lattice of TiO₂, [25,44] as no other peak was detected to indicate the existence of S^{2−} species in the TSC-600 as previously reported [44]. This is because it is easier to substitute the Ti⁴⁺ with S⁶⁺ than replace the oxygen atoms on the surface of TiO₂ by S^{2−}. The rationale behind this lies in: (1) S in the form of +6 (S⁶⁺) rather than in the form of −2 (S^{2−}) is provided by the used K₂S₆O₈, (2) the S^{2−} (1.7 Å) has larger ionic radius than O^{2−} (1.22 Å) making it difficult to dope anionic sulfur on TiO₂ due to the fact that large activation energy is required for the formation of Ti–S bond in the TiO₂, [44] and (3) the substitution of Ti⁴⁺ by S⁶⁺ is chemically more favorable than replacing O^{2−} with S^{2−}

owing to the requirement of lower formation energy [44,45]. As the calcination temperature greatly affects the oxidation state of S [46,47], therefore it is postulated that oxidation state of S in the TSC-600 should be comprised of an overlap of S⁶⁺ serving as the surface trap state for the photogenerated electrons and S⁴⁺ serving as the surface trap state for the photogenerated holes. This effect is of significant potential to suppress the recombination of electrons and holes thus advancing the photocatalytic activity [6].

The TEM images of TSC-400 at different magnifications were presented in Fig. 2a–f. From Fig. 2a to c, it is clear that the diameter of TSC-400 was around 50–100 nm. The TSC-400 displays porous structure which is comprised of different nanocrystals with a diameter of several nanometers. The distance among different nanocrystals is several nanometers, creating nanopores (primary pores as indicated in Fig. 2e). While the voids among the spheres also create pores, indicated as secondary pores in Fig. 2e [6]. Such a typical hierarchically meso/nanoporous structure is significantly

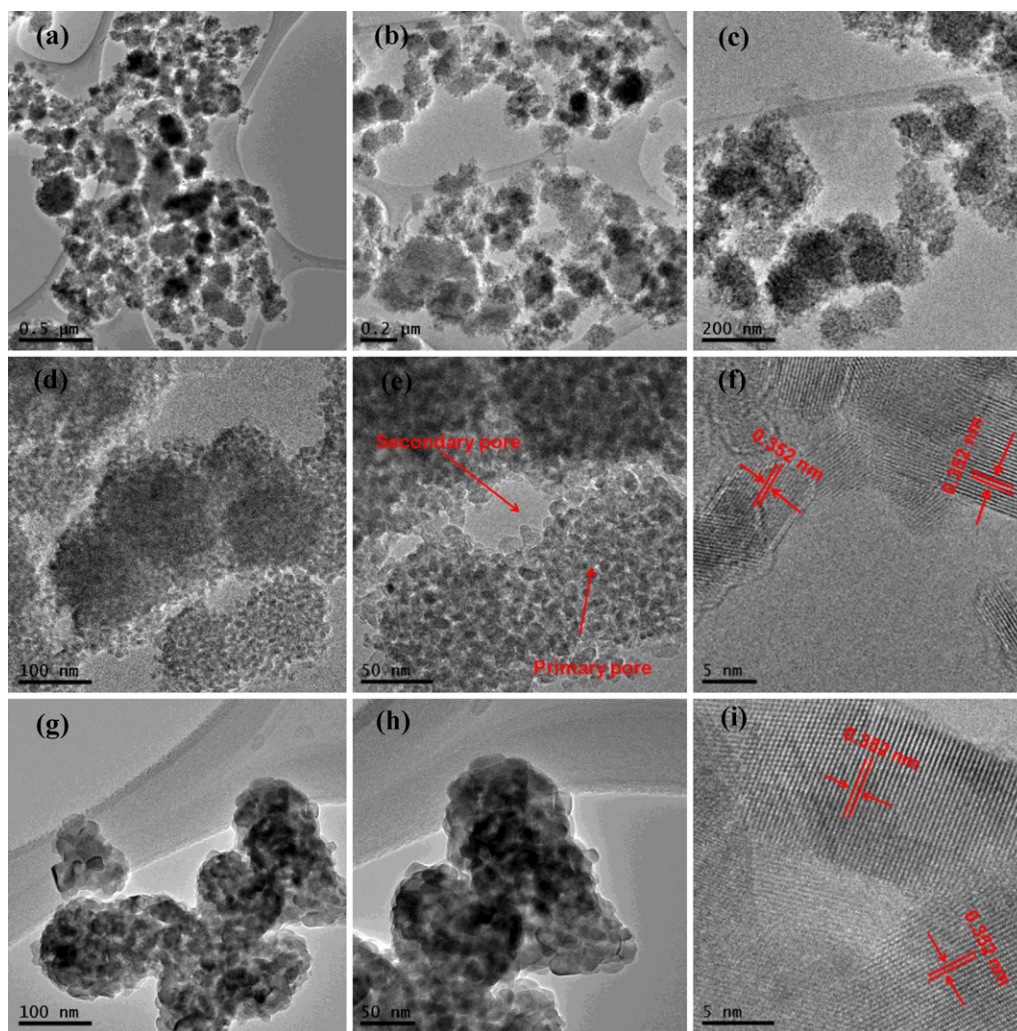


Fig. 2. (a)–(f) TEM images of the TSC-400 at different magnifications, and (g)–(i) TEM images of the TSC-600 at different magnifications.

favorable for the photocatalytic activity via creating more reaction sites encouraging the access of reactants into the desired places for the oxidative reactions taking place and permitting the multiple light scattering and reflection inside the interior [6,9]. A high resolution TEM image of the nanocrystal in TSC-400 is shown in Fig. 2f. The fringe lattice spacing of 0.352 nm is vividly visible, this is ascribed to the energetically stable crystal facet of TiO_2 (101) [9]. The TEM images of the TSC-600 are presented in Fig. 2g–i. Comparing the difference between Fig. 2d–f of TSC-400 and Fig. 2g–h of TSC-600, high temperature calcination would result in the shrinkage of nanopores among different TiO_2 nanocrystals, possibly because high temperature calcination would result in the aggregation of TiO_2 nanocrystals and thus reduce the specific surface area [48]. This is consolidated by the porous volume determined by N_2 adsorption/desorption isotherm in later section. What is more, the high resolution TEM image of the nanocrystals in the TSC-600 displays a typical fringe lattice spacing of 0.352 nm, ascribed to the energetically stable crystal facet of TiO_2 (101) [9]. Besides the TEM, FESEM was also employed to observe the morphology and its composition of S, and C codoped TiO_2 . From the FESEM images in Fig. 3a and b, it is clear to see the diameter of TSC-600 is around 100. The EDS spectrum in Fig. 3c further confirm that the element of O, Ti, C and S dominate the composition of the TSC-600. Meanwhile, the elemental mapping images of S (Fig. 3d), Ti (Fig. 3e), and O (Fig. 3f) reveal the uniform distributions of those elements

in the TiO_2 . This provides a solid proof that the S and C have been successfully codoped on the hierarchically meso/nanoporous TiO_2 .

The X-ray diffraction (XRD) is used to further investigate the crystal phase of the S- and C-codoped TiO_2 calcined at different temperatures. From the XRD patterns in Fig. 4a, it can be seen that low temperature calcination ($<200^\circ\text{C}$) was not able to result in well crystallization of TiO_2 . High temperature ($>200^\circ\text{C}$) calcination ensures the good crystallization of TiO_2 . The XRD patterns of the TSC-400, TSC-500 and TSC-600 exhibit typical peaks appearing at $2\theta = 25.38^\circ, 37.73^\circ, 48.16^\circ, 54.06^\circ$ and 55.29° which can be indexed to the (101), (004), (200), (105), and (211) crystal facets of anatase TiO_2 (PDF file 21-1272, JCPDS), respectively [9,24]. Furthermore, higher temperature calcination would enforce the intensities of those peaks thus favoring the photocatalytic activity. Except those typical peaks for anatase TiO_2 , the XRD pattern of TSC-800 also displays some new peaks at $2\theta = 27.44^\circ, 35.95^\circ, 41.29^\circ, 44.04^\circ, 54.19^\circ$ and 56.67° , indexing to the (110), (101), (111), (210), (211) and (220) crystal facets of rutile TiO_2 (JCPDS 89-0552), respectively [12]. This indicates that an even higher temperature ($>600^\circ\text{C}$) would result in the crystal phase transition of TiO_2 from anatase to rutile [47,49].

The UV–vis spectra of the prepared S- and C-codoped TiO_2 calcined at different temperatures was presented in Fig. 4b. The calcination temperature greatly relates to the UV–vis absorption capability of the S- and C-codoped TiO_2 . The TSC-0 and TSC-200

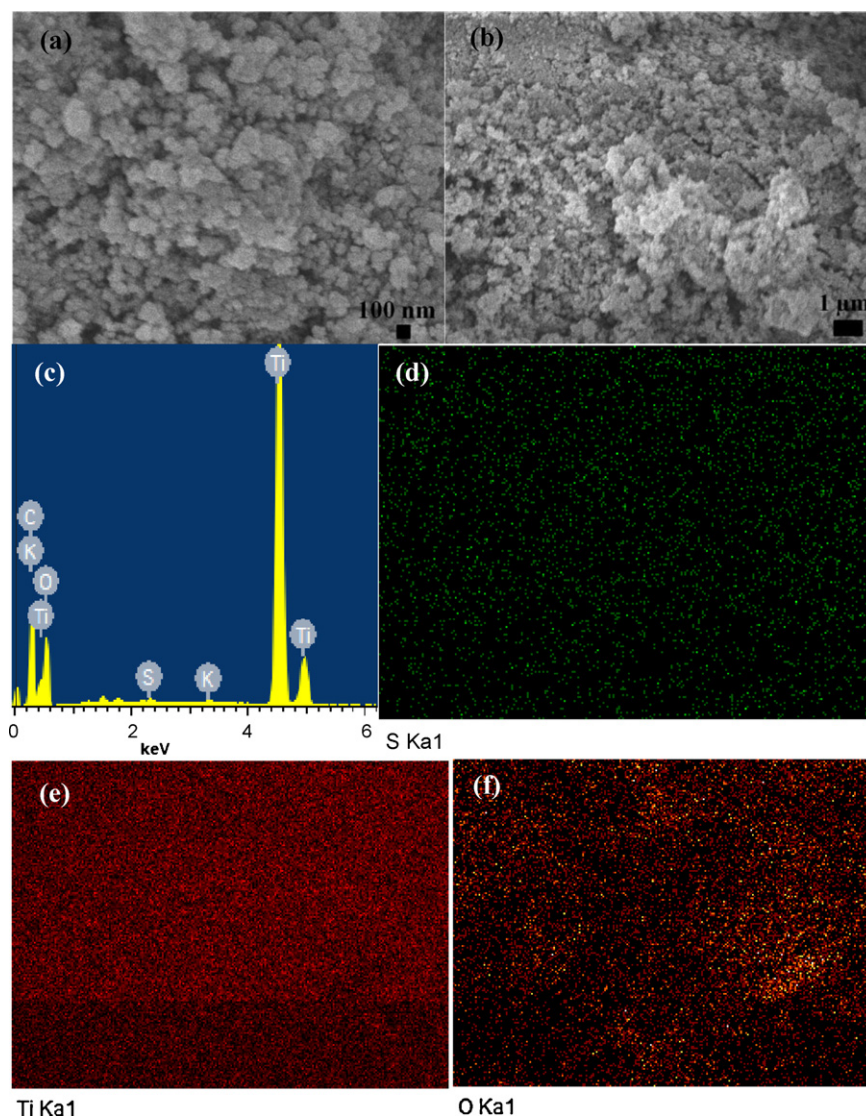


Fig. 3. (a)–(b) FESEM images, (c) EDS spectrum, and element mapping images (d) S, (e) Ti and (f) O of the TSC-600.

have the same diffuse reflectance spectra, while another three similar and slightly red-shifted spectra were corresponded to TSC-400, TSC-500 and TSC-600. This is because the high temperature calcination would be able to dope the S and C in the lattice of TiO_2 [6]. But the TSC-800 exhibits an even obvious red-shift of the absorption edge than the previous ones, this is resulted by

the transition of TiO_2 crystal phase from anatase to rutile [47]. The red-shift of the absorption edge and the transition of TiO_2 crystal phase all boost the improvement of photocatalytic activity [50].

The porous structure and the specific surface area of the S- and C-codoped TiO_2 calcined at different temperatures were characterized by nitrogen adsorption/desorption measurements. Calcination

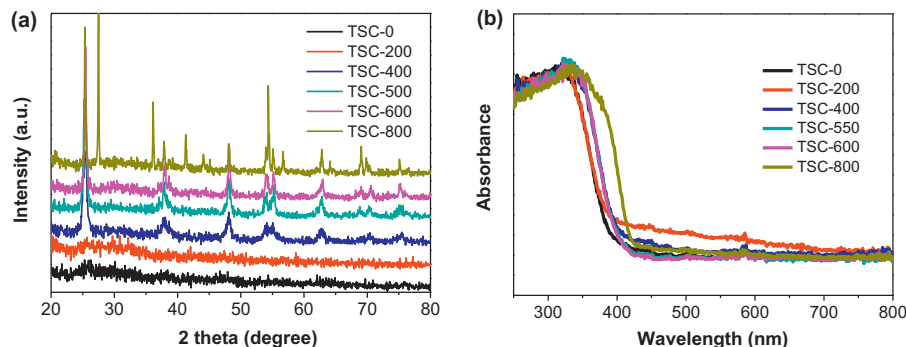


Fig. 4. (a) XRD patterns, and (b) UV-vis diffuse reflectance spectra of the prepared S- and C-codoped TiO_2 calcined at different temperatures.

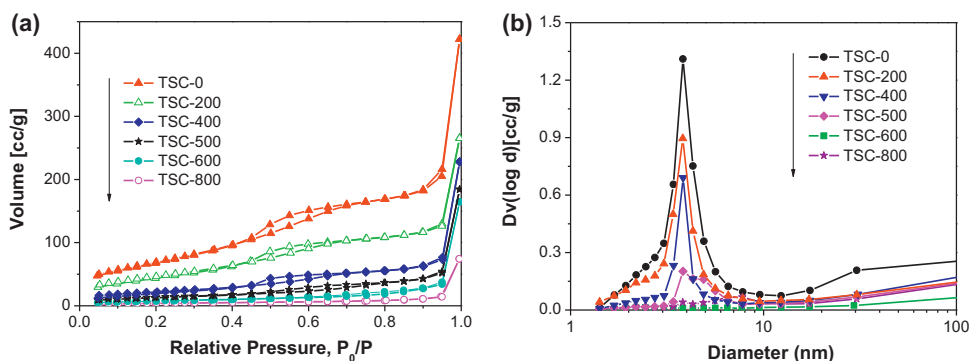


Fig. 5. (a) N₂ adsorption/desorption isotherm curves, and (b) BJH pore size distribution curves of the prepared S- and C- codoped TiO₂ calcined at different temperatures.

temperature also has a great influence on the isotherm behaviors of the S- and C-codoped TiO₂. All these samples showed typical IV-type isotherms (Fig. 5a) with two distinct capillary condensation steps, which indicated a bimodal pore-size distribution in primary nanoporous and secondary mesoporous regions [6]. An interesting phenomenon is that the rise of temperature would reduce the pore volume of those spheres, because of the reactant residuals being burnt off gradually. The corresponding BJH pore size distribution profiles of those S- and C-codoped TiO₂ calcined at different temperatures were presented in Fig. 5b. An obvious peak around 4 nm was observed for all the S- and C-codoped TiO₂ calcined at different temperatures, which reflects their nanoporous properties. But it should be noticed that there is an opposite relationship between the calcination temperature and the pore volume of the S- and C-codoped TiO₂. This is because pore volume was reduced after the reactant residuals filled in the TiO₂ spheres being burned off gradually. And high temperature calcination would promote the aggregation of TiO₂ nanocrystals into small particles thus causing the reduction of specific surface areas [48]. A descend trend of the specific surface areas for those S- and C-codoped TiO₂ was measured to be 257.1, 172.51, 79.51, 58.54, 28.57 and 14.32 m²/g corresponding to TSC-0, TSC-200, TSC-400, TSC-500, TSC-600 and TSC-800, respectively.

The photocatalytic H₂ generation activities of those S- and C-codoped TiO₂ were investigated in a water/methanol sacrificial reagent system under the irradiation of UV light [51]. The H₂ evolution volumes of the S- and C-codoped TiO₂ calcined at different temperatures were presented in Fig. 6a. Clearly, the S- and C-codoped TiO₂ exhibited high photocatalytic H₂ generation activity. The relationship between the H₂ evolution volume and the specific surface area of the S- and C-codoped TiO₂ corresponding to the calcination temperature was shown in Fig. 6b. Along with the increase of calcination temperature, the photocatalytic H₂ generation activity firstly increased to reach the maxima at 600 °C (TSC-600) and

then reduced. When the calcination temperature is less than 600 °C, the increase of calcination temperature would promote the crystallization of TiO₂ and enhance the light absorption capability, which naturally benefits the photocatalytic H₂ generation activity. When the calcination temperature is higher than 600 °C, the specific surface area is sharply reduced and becomes a dominant role in the reduction of photocatalytic H₂ generation activity. The balance point for specific surface area, crystallization and light absorption capability reaches at TSC-600, which displays the highest photocatalytic H₂ generation activity. Another important factor for TSC-600 with the highest photocatalytic activity lies in the element doping of S and C on TiO₂. The successful codoping of S and C on TiO₂ as verified by the XPS analysis in Fig. 1 not only accelerate the electron transfer but also create some active sites to trap the photogenerated electrons and holes to effectively suppress their recombination thus benefiting the photocatalytic activity. At the same time, the hierarchically meso/nanoporous property of TSC-600 would also greatly advance the photocatalytic activity via allowing more light reflection and absorption and easing the accessibility of reactants into the desired reaction sites. Such a balanced synergistic effect of S- and C-codoping on TiO₂ is easy for light reflection and suppressing the recombination of photogenerated electrons and holes, well crystallization, hierarchical meso/nanoporous property, eventually resulting in the highest photocatalytic H₂ generation activity for TSC-600.

For a further step, we also investigated the effect of Pt loading on the photocatalytic H₂ generation activity of hierarchically meso/nanoporous TiO₂ under the same testing conditions. The photocatalytic H₂ evolution curves of TSC-600 and 0.5% Pt/TSC-600 were shown in Fig. 7. Obviously, the Pt loading would enhance the photocatalytic activity of S- and C-codoped hierarchically meso/nanoporous TiO₂. The 0.5% Pt/TSC-600 generated about 1.5 times H₂ of TSC-600 under the same testing conditions. The 0.5% Pt/TSC-600 is a ternary system integrating the novel metal (Pt),

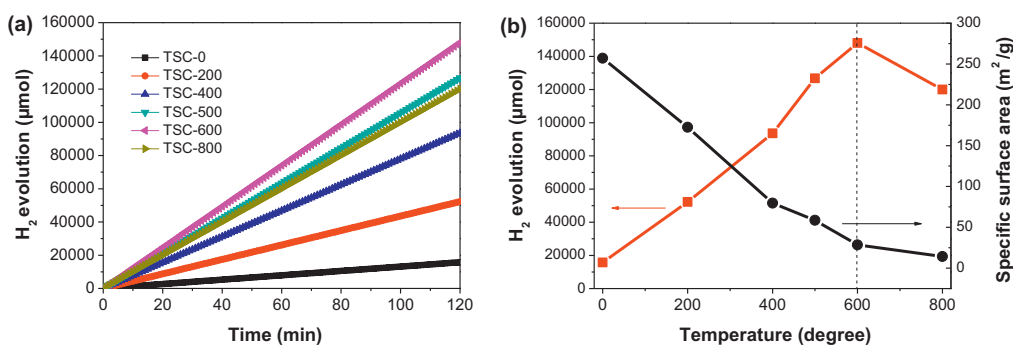


Fig. 6. (a) H₂ evolution curves of the S- and C-codoped TiO₂ calcined at different temperatures, and (b) the relationship between the H₂ generation activity and the specific surface area corresponding to the calcination temperature under the same conditions.

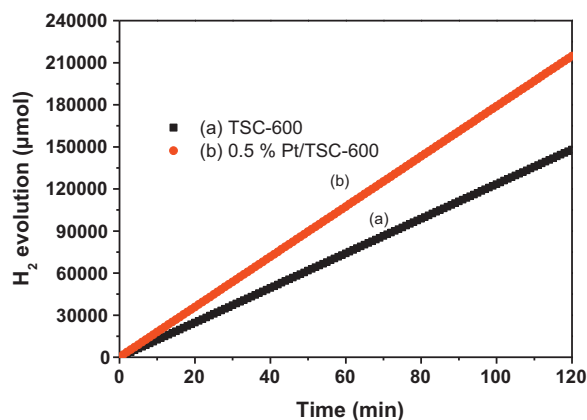


Fig. 7. H₂ evolution curves of TSC-600 and 0.5% Pt/TSC-600 under the same testing conditions.

semiconductor (TiO₂) and the inorganic elements (codoped S and C). In the original S- and C-codoped TiO₂, the S and C can not only accelerate the electron transfer but also create some active sites to trap the photogenerated electrons and holes to suppress their recombination [6]. The loaded Pt on hierarchical meso/nanoporous S- and C-codoped TiO₂ would further retard the recombination of photogenerated electrons and holes by forming a Schottky barrier at the Pt/TiO₂ interface, [52] and also would prevent the reverse reaction between O₂ and H₂ [31]. In such a way, the lifespan of photogenerated electrons and holes was maximized and thus leading to even higher photocatalytic H₂ generation activity in a comparison to TSC-600.

4. Conclusions

A facile hydrolysis-calcination synthetic strategy is developed to prepare a series of S- and C-codoped hierarchically meso/nanoporous TiO₂. The S- and C-codoped TiO₂ was well characterized by a variety of techniques such as XPS, TEM, FESEM, N₂ adsorption/desorption isotherm, etc. The photocatalytic activities of the S- and C-codoped TiO₂ were investigated in a water/methanol sacrificial reagent system under the irradiation of UV light. Calcination temperature greatly affects the crystallization, specific surface area, and the doping of S and C, finally influencing the photocatalytic H₂ generation activity. The S- and C-codoped TiO₂ calcined at 600 °C exhibits the highest H₂ generation activity, as a result of comprehensively competing effect of the doping of S and C to suppress the recombination of photogenerated electrons and holes, the crystallization, hierarchical meso/nanoporous property, specific surface area and enlarged light absorption capability. Furthermore, the 0.5% Pt/TSC-600 exhibited even higher photocatalytic H₂ generation activity than TSC-600 through further prolonging the lifespan of photogenerated electrons and holes and preventing the reverse reaction between H₂ and O₂.

References

- [1] J. Graciani, A. Nambu, J. Evans, J.A. Rodriguez, J.F. Sanz, *Journal of the American Chemical Society* 130 (2008) 12056–12063.
- [2] J. Yu, J. Ran, *Energy and Environmental Science* 4 (2011) 1364–1371.
- [3] Z. Liu, H. Bai, S. Xu, D.D. Sun, *International Journal of Hydrogen Energy* 36 (2011) 13473–13480.
- [4] S. Xu, J. Ng, X. Zhang, H. Bai, D.D. Sun, *International Journal of Hydrogen Energy* 35 (2010) 5254–5261.
- [5] A. Fujishima, K. Honda, *Nature* 238 (1972) 37–38.
- [6] P. Xu, T. Xu, J. Lu, S. Gao, N.S. Hosmane, B. Huang, Y. Dai, Y. Wang, *Energy and Environmental Science* 3 (2010) 1128–1134.
- [7] J.H. Pan, Z. Cai, Y. Yu, X.S. Zhao, *Journal of Materials Chemistry* 21 (2011) 11430–11438.

- [8] J.H. Pan, H. Dou, Z. Xiong, C. Xu, J. Ma, X.S. Zhao, *Journal of Materials Chemistry* 20 (2010) 4512–4528.
- [9] H. Bai, Z. Liu, D.D. Sun, *Applied Catalysis B: Environmental* 111–112 (2012) 571–577.
- [10] S. Yin, K. Ihara, Y. Aita, M. Komatsu, T. Sato, *Journal of Photochemistry and Photobiology A: Chemistry* 179 (2006) 105–114.
- [11] J.H. Pan, G. Han, R. Zhou, X.S. Zhao, *Chemical Communications* 47 (2011) 6942–6944.
- [12] H. Bai, Z. Liu, D.D. Sun, *Chemical Communications* 46 (2010) 6542–6544.
- [13] M.R. Hoffmann, S.T. Martin, W. Choi, D.W. Bahnemann, *Chemical Reviews* 95 (1995) 69–96.
- [14] X. Chen, S.S. Mao, *Chemical Reviews* 107 (2007) 2891–2959.
- [15] X. Chen, S. Shen, L. Guo, S.S. Mao, *Chemical Reviews* 110 (2010) 6503–6570.
- [16] A. Kudo, Y. Miseki, *Chemical Society Reviews* 38 (2009) 253–278.
- [17] H. Bai, Z. Liu, D.D. Sun, *Journal of Materials Chemistry* 22 (2012) 18801–18807.
- [18] X. Chen, C. Burda, *Journal of the American Chemical Society* 130 (2008) 5018–5019.
- [19] Z. Liu, D.D. Sun, P. Guo, J.O. Leckie, *Nano Letters* 7 (2007) 1081–1085.
- [20] X. Chen, L. Liu, P.Y. Yu, S.S. Mao, *Science* 331 (2011) 746–750.
- [21] Z. Wu, F. Dong, W. Zhao, H. Wang, Y. Liu, B. Guan, *Nanotechnology* 20 (2009) 235701.
- [22] C.K. Xu, Y.A. Shaban, W.B. Ingler, S.U.M. Khan, *Solar Energy Materials and Solar Cells* 91 (2007) 938–943.
- [23] G.S. Shao, L. Liu, T.Y. Ma, F.Y. Wang, T.Z. Ren, Z.Y. Yuan, *Chemical Engineering Journal* 160 (2010) 370–377.
- [24] H.J. Yun, H. Lee, J.B. Joo, N.D. Kim, M.Y. Kang, J. Yi, *Applied Catalysis B: Environmental* 94 (2010) 241–247.
- [25] D.I. Sayago, P. Serrano, O. Böhme, A. Goldoni, G. Paolucci, E. Román, J.A. Martiñ-Gago, *Surface Science* 482–485 (2001) 9–14.
- [26] R. Asahi, T. Morikawa, T. Ohwaki, K. Aoki, Y. Taga, *Science* 293 (2001) 269–271.
- [27] M. Sathish, B. Viswanathan, R.P. Viswanath, C.S. Gopinath, *Chemistry of Materials* 17 (2005) 6349–6353.
- [28] X. Yang, C. Cao, L. Erickson, K. Hohn, R. Maghirang, K. Klabunde, *Applied Catalysis B: Environmental* 91 (2009) 657–662.
- [29] W.J. Ren, Z.H. Ai, F.L. Jia, L.Z. Zhang, X.X. Fan, Z.G. Zou, *Applied Catalysis B: Environmental* 69 (2007) 138–144.
- [30] R. Hahn, F. Schmidt-Stein, J. Salonen, S. Thiemann, Y. Song, J. Kunze, V.-P. Lehto, P. Schmuki, *Angewandte Chemie International Edition* 48 (2009) 7236–7239.
- [31] J. Yu, L. Qi, M. Jaroniec, *Journal of Physical Chemistry C* 114 (2010) 13118–13125.
- [32] L. Liu, H. Liu, Y.-P. Zhao, Y. Wang, Y. Duan, G. Gao, M. Ge, W. Chen, *Environmental Science and Technology* 42 (2008) 2342–2348.
- [33] S. Song, Z. Liu, Z. He, A. Zhang, J. Chen, Y. Yang, X. Xu, *Environmental Science and Technology* 44 (2010) 3913–3918.
- [34] T. Zhao, Z. Liu, K. Nakata, S. Nishimoto, T. Murakami, Y. Zhao, L. Jiang, A. Fujishima, *Journal of Materials Chemistry* 20 (2010) 5095–5099.
- [35] G. Colon, M.C. Hidalgo, G. Munuera, I. Ferino, M.G. Cutrufello, J.A. Navio, *Applied Catalysis B: Environmental* 63 (2006) 45–59.
- [36] H. Bai, J. Juay, Z. Liu, X. Song, S.S. Lee, D.D. Sun, *Applied Catalysis B: Environmental* 125 (2012) 367–374.
- [37] H. Bai, Z. Liu, D.D. Sun, *Physical Chemistry Chemical Physics* 13 (2011) 6205–6210.
- [38] Y. Zhao, X. Zhang, J. Zhai, J. He, L. Jiang, Z. Liu, S. Nishimoto, T. Murakami, A. Fujishima, D. Zhu, *Applied Catalysis B: Environmental* 83 (2008) 24–29.
- [39] J.H. Pan, X. Zhang, A.J. Du, D.D. Sun, J.O. Leckie, *Journal of American Chemical Society* 130 (2008) 11256–11257.
- [40] Z. Liu, D.D. Sun, P. Guo, J.O. Leckie, *Chemistry – An European Journal* 13 (2007) 1851–1855.
- [41] X.J. Zheng, L.F. Wei, Z.H. Zhang, Q.J. Jiang, Y.J. Wei, B. Xie, M.B. Wei, *International Journal of Hydrogen Energy* 34 (2009) 9033–9041.
- [42] S. Xu, A.J. Du, J. Liu, J. Ng, D.D. Sun, *International Journal of Hydrogen Energy* 36 (2011) 6538–6545.
- [43] S. Xu, D.D. Sun, *International Journal of Hydrogen Energy* 34 (2009) 6096–6104.
- [44] Q. Xiang, J. Yu, M. Jaroniec, *Physical Chemistry Chemical Physics* 13 (2011) 4853–4861.
- [45] J.C. Yu, W. Ho, J. Yu, H. Yip, P.K. Wong, J. Zhao, *Environmental Science and Technology* 39 (2005) 1175–1179.
- [46] T. Ohno, M. Akiyoshi, T. Umebayashi, K. Asai, T. Mitsui, M. Matsumura, *Applied Catalysis A: General* 265 (2004) 115–121.
- [47] Q. Xiao, L. Ouyang, *Chemical Engineering Journal* 148 (2009) 248–253.
- [48] Y. Noda, B. Lee, K. Domen, J.N. Kondo, *Chemistry of Materials* 20 (2008) 5361–5367.
- [49] M. Hamadani, A. Reisi-Vanani, A. Majedi, *Applied Surface Science* 256 (2010) 1837–1844.
- [50] Z. Liu, X. Zhang, S. Nishimoto, M. Jin, D.A. Tryk, T. Murakami, A. Fujishima, *Langmuir* 23 (2007) 10916–10919.
- [51] S.S. Lee, H. Bai, Z. Liu, D.D. Sun, *International Journal of Hydrogen Energy* 37 (2012) 10575–10584.
- [52] A. Patsoura, D.I. Kondarides, X.E. Verykios, *Applied Catalysis B: Environmental* 64 (2006) 171–179.